Multiscale numerical optimisation of hybrid metal/nonwoven shields for ballistic protection

Multiscale numerical optimisation of hybrid metal/nonwoven shields for ballistic protection

J. Vila-Ortega[1], A. Ridruejo[1], F. Martínez-Hergueta[2]

[1] *Department of Materials Science, Universidad Politécnica de Madrid, E. T. S. de Ingenieros de Caminos. 28040 - Madrid, Spain.*

[2] *School of Engineering, Institute for Infrastructure and Environment, University of Edinburgh, William Rankine Building, EH9 3FG, Edinburgh, UK.*

Abstract

This research presents a detailed numerical study of the ballistic performance of lightweight hybrid metal/nonwoven shields for automotive applications. Several configurations, including different number of nonwoven fabrics, were analysed to find the optimal design. Impact response of the nonwoven fabric was predicted by a multiscale numerical constitutive model able to capture its complex deformation and failure mechanisms: fibre straightening, realignment and disentanglement. Special attention was paid to the interaction between layers for different air gaps in the final energy absorption capacity of the shield, and detailed analysis of the different sequences of triggered failure modes was provided. The hybrid shield outperformed the previous configurations, resulting in an absorption capacity about twice the sum of the energies dissipated by the steel plates and the nonwovens individually. Furthermore, the hybrid shield increased the energy absorption capacity of the baseline steel plates by a factor over 8, with an almost negligible increment of areal weight of 5.5%, giving the possibility to improve the ballistic performance of conventional automotive components without penalising the fuel consumption of the vehicle.

Keywords: Ballistics, hybrid shields, nonwoven, finite element simulation

1. Introduction

During the last years, awareness of ballistic protection has been raised in the automotive industry. Although armoured vehicles have been extensively explored for defence [8, 19], the

high areal weight of conventional metal barriers penalises manoeuvrability and hinders their implementation in the civilian automotive sector, where low fuel consumption and carbon emissions are a priority. Areal weight can be drastically reduced by combining different materials in a shield, taking advantage of the synergistic energy dissipation capability of each component [21, 35, 34, 49]. As an example, the use of fibre-metal laminates is extended from the aerospace sector to marine or civil engineering applications, where materials such as GLARE are used for ballistic and blast protections [43, 38, 50, 14, 2]. For lower impact energies, associated to smaller calibres and fragments, dry fabrics with 100% content high strength fibres offer a lightweight solution. Polymeric fibres such as aramids (e.g. Kevlar) and ultra-high molecular weight polyethylene (Dyneema) are now able to double the tensile strength of high-strength steel, with one fifth of the areal weight of the metal plate [15, 1]. Depending on the disposition of the fibres in the material, they can be classified in woven or nonwoven fabrics. In the former, fibres are bundled in weave yarns following a regular pattern, while fibres form a disordered network in the latter [37]. Both materials are used in ballistic protection [9, 33, 45, 7], however, the best performance against small fragments is provided by nonwovens [4, 18, 47].

Hybrid metal/dry fabric shields are an innovative lightweight solution to arrest projectiles. This system provides sufficient structural rigidity for components subjected to impact loads and has been recently used for civil applications such as turbine engine fragment barriers [42, 44]. Dry fabrics are usually placed in the front face of the target to redistribute the load over the metal plate, changing the failure mode from plugging to petalling [15]. They are also placed in the rear face to absorb significant amount of energy by tensile deformation [5, 16]. Hybrid shields are usually combined with air gaps to improve the ballistic performance [13, 46, 12]. Air gaps reduce the bending stiffness of the plates, changing their failure mechanisms from shear to tensile modes, therefore, increasing the dissipated energy compared to their bulk laminate counterparts. Considering the complexity of the interaction between different plates and materials, numerical simulations are usually employed to provide a thorough insight of the coupled failure mechanisms [24, 25]. Finite element analysis is a powerful tool which allows to explicitly combine all the target components and analyse

the failure sequence, with a higher accuracy than the one offered by high speed imaging.

It is possible to find multiple studies of metal/dry woven fabric shields in the literature, however, to the authors' knowledge, there are no applications for their counterpart metal /nonwoven combination. In comparison, nonwoven fabrics present lower stiffness and strength but higher deformability than their woven counterparts, resulting in an excellent performance for small calibres and fragments. One of the reasons that hindered the integration of nonwoven materials into ballistic protections was the lack of understanding of their micromechanical response, which resulted in low accuracy of the prediction of their ballistic performance. Micromechanisms of deformation and fracture depend on the interaction of a number of factors including fibre uncurling, fibre reorientation as well as fibre sliding and disentanglement, which are difficult to be captured by classical phenomenological constitutive models [7]. Recent multiscale modelling efforts focused on the simulation of needle-punched ultra-high molecular weight polyethylene nonwovens, providing a validated simulation framework to accurately predict the ballistic response of the material in terms of energy absorption and failure micromechanisms [30, 31]. These constitutive models were recently employed to simulate the response of hybrid woven/nonwoven shields, showing the potential of nonwovens to improve the ballistic performance of conventional barriers with minimal increment in areal weight [32].

Considering the potential of nonwovens to improve the ballistic performance of conventional components in the automotive sector, this investigation aims to provide a deeper understanding on the ballistic performance of hybrid metal/nonwoven shields considering several design parameters such as number of layers and air gaps. A virtual testing framework by means of the Finite Element Method was developed to perform rigorous parametrical studies. A conventional vehicle door composed by two thin steel plates was taken as baseline configuration for this study. To this end, steel plates and nonwovens were modelled, individually or in multilayer configurations, to characterise their ballistic response. Special attention was paid to the interaction between layers in the final energy absorption capacity of the target. The influence of the spacing was analysed for 2 and 3 nonwoven layers targets on a wide range of distances, from 0.1 to 50 mm, showing the difference in ply

interaction, failure sequences and energy transfer mechanisms. The optimal configuration was finally used to simulate the ballistic response of a hybrid metal/nonwoven vehicle door composed by two external steel plates and three internal nonwovens. Ballistic performance was analysed in terms of ballistic limit, energy absorption capacity and residual velocity curves, showing the benefits of the hybrid configuration over the single material targets.

2. Materials

Two materials have been selected for the following study: an ultra-high molecular weight polyethylene needle-punched nonwoven fabric and a commercial steel (ArcelorMittal 260BH) for automotive industry. The resin free needle-punched nonwoven dry fabric is denominated Fraglight NW201 (DSM) and it is manufactured by the continuous deposition of single filaments of ultra high molecular weight polyethylene (Dyneema SK75) of approximately 60 mm in length on a moving bed surface forming a batt. The batt is needlefelted with the aid of the oscillatory application of barbed needles, which introduce mechanical entanglements among fibres [37]. The nominal areal density and thickness of the fabric, as given by the manufacturer, are ≈190-220 g/m^2 and ≈1.5 mm, respectively.

The needlepunched process introduced two principal material orientations denominated machine (MD) and transverse (TD) directions, which follow the bed displacement and its orthogonal, respectively. The initial fibre orientation distribution function (ODF) was analysed in detail by means of 3D X-ray computed tomography (XCT) and 2D wide angle X-ray diffraction (WAXD) and it was found to be isotropic [29]. Fibres were initially curved and load was transferred within the fabric through the random and isotropic network of knots created by needle-punching, leading to the formation of an active fibre network, see Fig.1(a). Uncurling and stretching of the active fibres was followed by fibre sliding and pull-out from the entanglement points. Most of the strength and energy dissipation was provided by the extraction of the active fibres from the knots and final fracture occurred by the total disentanglement of the fibre network in a given section at which the macroscopic deformation was localized. Although the initial fibre ODF was isotropic, the in-plane mechanical properties were highly anisotropic: the stiffness, strength and energy dissipated upon tensile deforma-

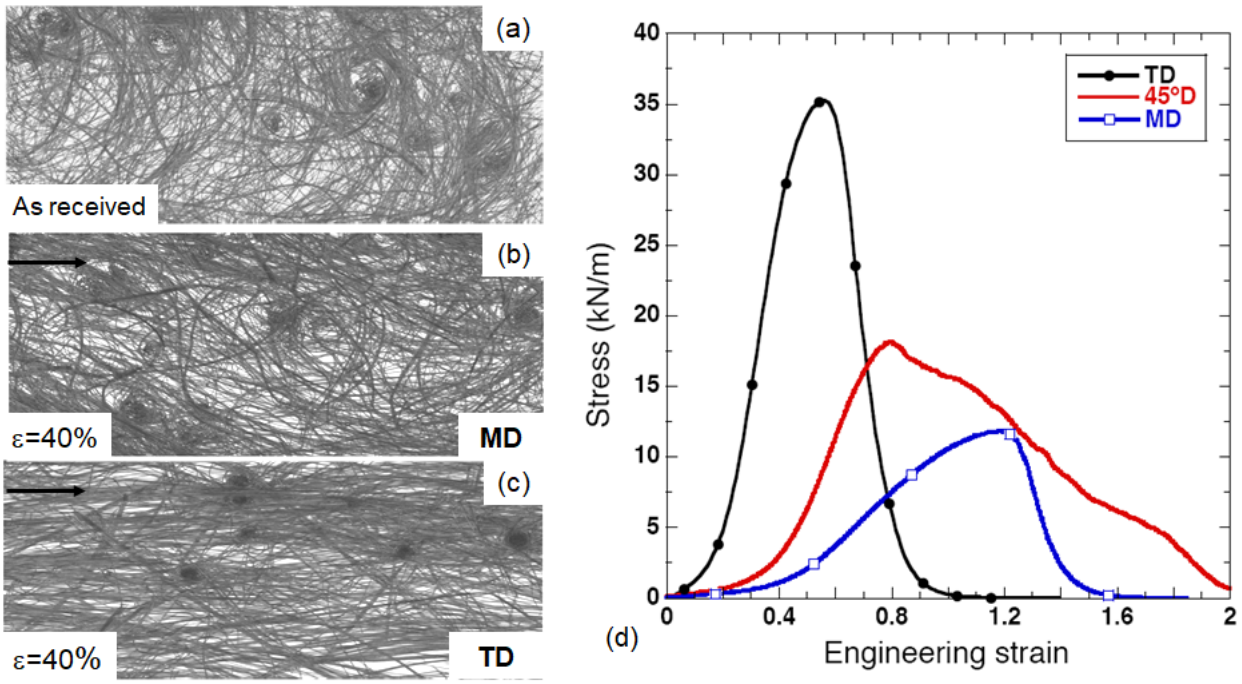

Figure 1: Evolution of the fibre ODFs of the nonwoven fabric with deformation. (a) As-received material, (b) after 40% of deformation along MD and (c) after 40% of deformation along TD. (d) Representative nominal stress (load per unit width) *vs.* engineering strain tensile curves in the fabric plane along the transverse direction (TD) and the machine direction (MD). Tests were carried out in square specimens of 100 x 100 mm^2 under quasi-static loading conditions [29].

tion in the TD were 2-3 times higher than those along MD, while the strain at maximum load along TD was only one half of that along MD, see Fig.1(d). This anisotropic behaviour was dictated by the microstructure evolution. Fibres tended to align towards the loading direction when the fabric was deformed along TD but minor fibre ODF evolution was appreciated during deformation along MD. Micromechanical pull-out tests indicated that the structure of the knots connected more fibres along TD than along MD and the better fibre interconnection led to a larger active fibre skeleton, enhancing the mechanical response along TD. In terms of affinity, fabrics deformed along TD essentially displayed affine deformation –i.e. most of the macroscopic strain was transferred to the fibres by the surrounding fabric–, while MD-deformed fabrics underwent non-affine deformation, and most of the macroscopic strain was not transferred to the fibres. Further information can be found in [29].

The ballistic performance of the nonwoven fabrics was characterized in detail in a previous publication [28]. The nonwoven dissipated the energy of the projectile by in-plane deformation of the fabric leading to a cone of deformed material with an elliptical cross-section due to the different wave propagation velocities along MD and TD, see Fig.2. The deformation was accommodated by the same mechanisms observed during quasi-static in-plane tensile deformation: load was transferred within the fabric through the random fibre network, which included uncurling and rotation of the active fibres in the connected skeleton followed by fibre sliding and pull-out from the entanglement points leading to a permanent global deflection of the target until the projectile was arrested. In the tests carried out above the ballistic limit, the final penetration of the target was accomplished by tearing as the fibres were pulled out from the entanglement points and damage was localized around the projectile.

The second material selected for this feasibility study was a commercial bake hardening steel 260BH for automotive industry manufactured by Arcelor-Mittal [3]. Bake hardening steels have been designed specifically for structural applications such as underbody or reinforcement of lining. They promoted a significant increase in yield strength during low-temperature heat treatments, particularly paint curing at 170 °C approximately, which resulted in substantial weight reduction in all finished parts in the case of low forming strains. They also possessed high deformability and improved dent resistance, which made them suitable for impact applications. 0.7 mm thickness plates were chosen for the proposed study, representative of the real thickness of a car door with a density of 7850 kg/m^3 and an equivalent areal weight of 5500 g/m^2.

3. Computational modelling of impact on hybrid shields

Numerical simulations of the ballistic impact on the steel plates, the nonwoven fabrics and the multi-layered hybrid shield were performed to get a better understanding of the deformation and fracture mechanisms during impact and optimise the ballistic performance. Simulations were carried out using the finite element method in Abaqus/Explicit within the framework of large displacements and rotations with the initial unstressed state taken as

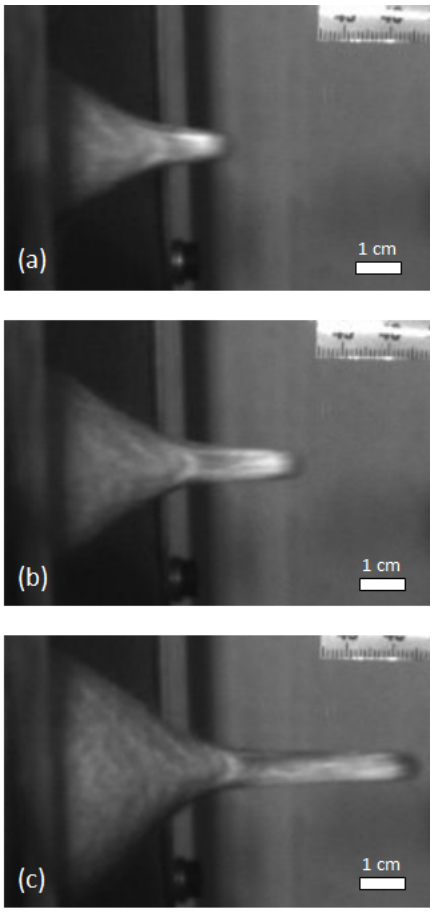

Figure 2: Deformation of the polyethylene nonwoven fabric during impact at 322 m/s, above the ballistic limit. (a) $t = 150$ μs, (b) $t = 225$ μs and (c) $t = 350$ μs. Failure mode of the material was fibre disentanglement. [28]

reference. Different constitutive material models were used to describe the steel plates and the nonwoven fabrics as detailed below.

3.1. Constitutive model of steel plates

Bake hardening steel, after treatment, possess little strain rate sensitivity [10], so a standard isotropic linear hardening model (with Von Mises yield surface), available in the Abaqus/Explicit material library [11] was employed:

$$\sigma_y = \sigma_y^0 + H\varepsilon^{pl} \tag{1}$$

where σ_y defined the yield stress, σ_y^0, its initial value, ε^{pl} the plastic deformation and H the hardening modulus. The elastic Young's Modulus, E, and the Poisson's ratio, ν, were also defined to compute the recoverable strains.

Failure of the material was established by the ductile failure criterion proposed in [17, 20], a phenomenological model for predicting the onset of damage due to nucleation, growth and coalescence of voids. The model assumed that the equivalent plastic strain at the onset of damage, $\overline{\varepsilon}_D^{pl}$, was a function of strain rate $\dot{\varepsilon}^{pl}$ and stress triaxiality ξ. In the particular case of the 260BH steel, a rate independent curve was defined with the tabular set of parameters included in Table 1.

The criterion for damage initiation was met when the following condition was satisfied:

$$\int \frac{d\overline{\varepsilon}^{pl}}{\overline{\varepsilon}_D^{pl}} = 1 \tag{2}$$

After the onset of damage, degradation of the material occurred. Numerically, it was implemented as a softening of the undamaged stress tensor, $\overline{\boldsymbol{\sigma}}$, such as:

$$\boldsymbol{\sigma} = (1-d)\overline{\boldsymbol{\sigma}} \tag{3}$$

The damage variable, d, ensured that the total energy dissipated after the onset of damage was equal to the fracture toughness of the alloy, Γ . To avoid any mesh dependency, the dissipated energy was normalised by the characteristic length of the finite element, L_{ch}:

$$\Gamma = \int_{\overline{\varepsilon}_0^{pl}}^{\overline{\varepsilon}_f^{pl}} L_{ch}\sigma_y d\varepsilon^{pl} = \int_0^{\overline{u}_f^{pl}} \sigma_y d\overline{u}^{pl} \tag{4}$$

where $\overline{u}^{pl}$ stands for the equivalent plastic displacement, the fracture work conjugate of the yield stress after the onset of damage. The definition of the damage variable considering exponential softening was given as:

$$d = 1 - exp\left(-\int_0^{\overline{u}_f^{pl}} \frac{\overline{\sigma}_y \dot{\overline{u}}^{pl}}{\Gamma}\right) \tag{5}$$

where $\dot{\overline{u}}^{pl}$ stands for the evolution of plastic displacement, and $\overline{\sigma}_y$ for the trial yield strength. Further information about the material model is available in [11] and material properties are summarized in Table 1. More details of the implementation are available in [48].

Table 1: Material parameters for Steel 260BH [48].

Density, ρ	7850 kg/m^3
Young's Modulus, E	200 GPa
Poisson's ratio, ν	0.27
Hardening Modulus, H	2.5 GPa
Ultimate Strength, σ_0	400 MPa
Yield Strength, σ_y	280 MPa
Strain to failure, ε_D^{pl}	0.3
Strain rate, $\dot{\varepsilon}^{pl}$	10^6
Triaxiality, ξ	0.8
Fracture toughness Γ	0.072 J/mm^2

3.2. Constitutive model of nonwoven fabrics

The mechanical behaviour of the nonwoven fabric was given by a multiscale constitutive model previously developed, which was able to take into account the complex deformation and fracture mechanisms of this material under in-plane deformation and impact [30, 31]. The model provided the mechanical response of a mesodomain of the nonwoven fabric, which corresponded to a finite element in the numerical simulation, and it is briefly recalled here for the sake of completion.

The model was divided in two blocks which dealt with the network and the fibre response. The network model established the relationship between the macroscopic deformation gradient $\mathbf{F}$ and the microscopic response obtained by integrating the response of the fibres in the mesodomain that was formed by a planar square region of arbitrary size containing a random network of long, curly, non-interacting fibres, see Fig.3. The mechanical response of the mesodomain in terms of the second Piola-Kirchoff nominal stress tensor, $\mathbf{S}$, (force per unit width) was given by

$$\mathbf{S} = \int_{-\frac{\pi}{2}}^{\frac{\pi}{2}} \Psi(\beta_0)\sigma_f(\lambda)f_f(\beta_0)\frac{(\hat{\mathbf{n}}\otimes\hat{\mathbf{n}})}{\sqrt{\mathbf{C}\hat{\mathbf{n}}\cdot\hat{\mathbf{n}}}}\,d\beta_0 \tag{6}$$

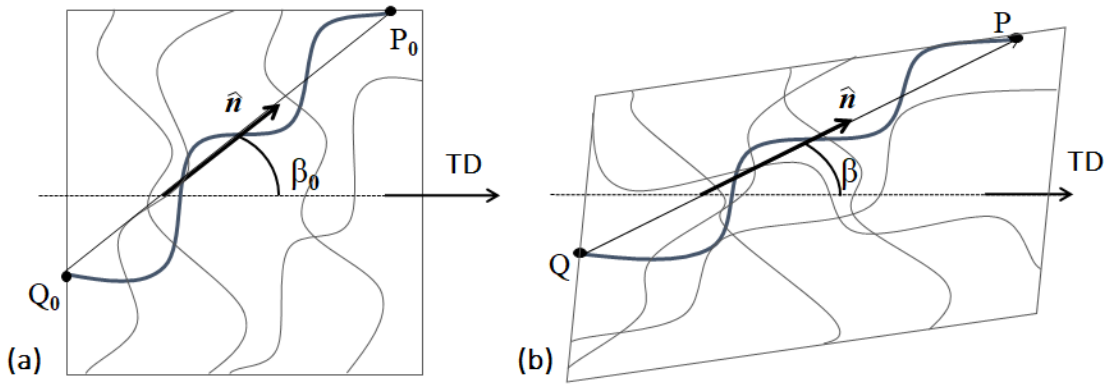

Figure 3: Schematic of the network mesodomain formed by different sets of curly fibres. (a) References and (b) deformed configurations [30].

where $\Psi(\beta_0)$ was the fibre orientation distribution function (ODF) in the reference configuration, $\sigma_f(\lambda)$ the stress carried by the fibre as a function of the stretch λ, $f_f(\beta_0)$ the active fibre length engaged in the deformation process, $\mathbf{C} = \mathbf{F}^T\mathbf{F}$ the right Cauchy-Green strain tensor, and $\hat{\mathbf{n}}$ a unit vector which formed an angle β_0 with respect to an arbitrary, privileged direction (e.g. the transverse direction TD of the nonwoven fabric) in the initial configuration.

The fibre model took into account the deformation features experimentally found for each set of fibres, including fibre uncurling and re-orientation, non-affine deformation, pull-out and disentanglement [29]. These mechanisms were introduced in a phenomenological model which characterised the stress (σ_f) - stretch (λ) behaviour of the fibre according to:

$$\begin{aligned} \sigma_f &= K\left[\eta(\beta_0)(\lambda-1)\right]^3 \qquad \sigma_{tr} < \sigma_{po} \\ \sigma_f &= (1-d)K\left[\eta(\beta_0)(\lambda-1)\right]^3 \quad \sigma_{tr} > \sigma_{po} \end{aligned} \tag{7}$$

where K was the fibre stiffness, $\eta(\beta_0)$ was the affinity parameter, which measured the percentage of macroscopic deformation transmitted into the microstructure along each direction, σ_{po} the pull-out strength, d the damage parameter that accounted for the progressive reduction in the load carried by the fibre during extraction from the fabric and σ_{tr} was a trial stress computed from the fibre stretch assuming no damage.

Once the fibre stress had attained the pull-out strength, σ_{po}, the pull-out process begun

and the load carried by the fibre decreased progressively until it was completely disengaged from the fabric. The stress carried by the fibres during this stage was determined by means of a continuum damage model, and it was function of the damage parameter d and of the fracture energy per unit fibre cross-section dissipated during pull-out, G. This fracture energy was obtained from the belt friction theory, and it was given by [30],

$$G = \frac{\sigma_{po} L_c}{\mu\theta}\left(1 - e^{-\mu\theta m_{po}}\right) \tag{8}$$

where L_c was the fibre length between entanglements, μ the friction coefficient, θ the fibre curvature and m_{po} the number of mechanical entanglements involved in the pull-out process.

In each time increment of the numerical simulation, the right stretch tensor $\mathbf{U}$ was used to compute the stretch λ of each set of fibres. Each mesodomain of the fibre network (that coincides with a finite element with one Gauss point) was described by 65 sets of fibres with different orientation in the range $(\frac{-\pi}{2}, \frac{\pi}{2})$ and the second Piola-Kirchoff nominal stress tensor, $\mathbf{S}$, was obtained by integrating eq.(6) along the different orientations. The fibre stretch λ for each fibre set was used to compute the trial stress σ_{tr} in the absence of damage, which was compared with the corresponding pull-out strength σ_{po}. The pull-out strength for each fibre set was chosen at the beginning of the simulation using a Monte Carlo lottery inside a given interval. If $\sigma_{tr} \leq \sigma_{po}$, $\sigma_{tr} = \sigma_f$ according to equation (7). If $\sigma_{tr} > \sigma_{po}$, the actual fibre stress σ_f was obtained from a continuum damage model depending on the damage variable d and the fracture energy, G, following eq. (7). A damage variable D was defined for each finite element (Gauss point) as the average damage of all fibre sets in the elements. The details of the numerical implementation of the damage model as well as of the crack band approach to obtain results that are independent of the finite element size can be found in [30]. The constitutive model parameters can be found in Table 2 and coincide with those used in previous investigations to predict the impact behaviour of the nonwoven fabric [27, 31, 32].

Table 2: Model parameters [30].

Fibre density, ρ_f	970 kg/m^3
Fibre length, L_{fiber}	60 mm
Bundle cross section, Ω	1.27 10^{-4} mm^2
Areal density, ρ	0.2 kg/m^2
Friction coefficient [40], μ	0.1
Initial fibre ODF, $\Phi(\beta_0)$	$1/\pi$
Initial fibre curvature, θ_0	π rad
Affinity, $\eta(\beta_0)$	Interpolation [1, 1/2] [30]
Active fibre length, $f_f(\beta_0)$	$0.223\eta(\beta_0)$-0.084 mm
Fibre stiffness, K	9.0 GPa
Pull-out strength, σ_{po}	[0.3, 1.7] GPa
Contour length, L_c	2.0 mm
Fibre pull-out length, L_{po}	60 mm
Critical value of the hydrostatic strain, ($\hat{U}_{unl}$)	0.85

3.3. Numerical implementation and virtual impact testing

Steel plates and nonwoven layers were simulated individually and combined in hybrid configurations to virtually optimise the ballistic performance of the hybrid metal/nonwoven shield. Targets had a square shape of 350 x 350 mm^2 and all the lateral boundaries were fully constrained during the impact simulation. The mesh was finer around the impact zone (finite elements of 1 mm^2) and the element size increased progressively with the distance towards the clamped edges to reduce the computational cost. Steel plates were discretised with S4R shell elements, reduced integration, hourglass control and finite membrane strain, meanwhile nonwoven fabric layers were simulated by M3D4R membrane elements, reduced integration, enhanced hourglass control and second order accuracy. Default Abaqus bulk viscosity was used to minimise numerical instabilities. The used of membrane elements to simulate the mechanical response of dry woven fabrics has been previously validated [23, 41]

and it is also a conventional approach to study nonwoven materials [6, 26, 31, 36]. The impactor was modelled as a rigid sphere of 5.5 mm in diameter, density 7.85 g/cm^3 and 0.706 g of mass. Contact between the different layers and the impactor was defined by a softened tangential behaviour with an sticking friction slope of κ= 0.001 and a friction coefficient μ=0.1. Fully damaged elements ($D > 0.99$), were removed from the simulations to avoid excessive element distortion. In the particular case of the metal plates, the damage model available in Abaqus deleted the elements once the damage parameter achieved a value equal to 0.99 [11]. In the case of the VUMAT subroutine for the nonwoven, elements were deleted when the average damage variable (computed from the 65 individual fibre sets at each Gauss point) achieved a value equal to 0.99.

The developed virtual testing framework was employed to accomplish a rigorous optimisation exercise of the hybrid shields, focusing on the influence of the relative distance of the nonwoven fabrics on the ballistic performance. Numerical simulations and tested configurations are summarised in Table 3. First of all, the impact response of the steel plate and the nonwoven fabric were analysed separately to determine their deformation and failure mechanisms. Predictions of the ballistic performance of the nonwoven fabric were correlated against previous experimental results [28]. Afterwards, parametrical studies on the relative spacing between nonwoven layers were accomplished to determine the influence on the final energy absorption capacity of the targets. Dependency of the energy dissipation with the spacing between layers was characterised for a target consisting of two nonwoven layers with variable spacing in the interval 0.1 to 50 mm every 2 mm at a fix impact velocity of 450 m/s, above the ballistic limit. Furthermore, ballistic limit and residual velocity curves for selected spacings of 0.1, 10 and 50 mm were obtained for comparison purposes. This study was additionally extended for three-layer systems with 10 mm spacing. Finally, a hybrid shield consisting of 2 external steel plates with 3 internal nonwoven layers was analysed to determine the deformation mechanisms and ascertained the benefits of the hybrid system over the single material targets due to the interaction between layers. Distance between the steel plates and the nonwoven was set to 30 mm. Meanwhile, nonwovens were regularly spaced every 10 mm, resulting on a final shield thickness of 80 mm and a total areal weight

Table 3: Summary of tested configurations and numerical results.

Shield	Air gap (mm)	Areal density (g/m^2)	V_{50} (m/s)	Energy at V_{50} (J)
1 steel plate	—	5500	165	9.6
2 steel plates	80	11000	235	19.5
1 nonwoven	—	200	328	37.9
2 nonwovens	0.1	400	420	62.3
2 nonwovens	10	400	436	67.1
2 nonwovens	50	400	409	59.1
3 nonwovens	10	600	507	94.5
Hybrid	30/10/10/30	11600	745	195.9

of 11600 g/m^2.

Comparison of the different targets was carried out in terms of ballistic limit V_{50}, maximum energy absorption capacity and residual velocity curves obtained from an average of 8 simulations at different impact velocities. Relationship between the ballistic limit and the residual velocity was established by the Lambert-Jonas equation [22],

$$V_{res} = A(V_{ini}^n - V_{50}^n)^{1/n} \tag{9}$$

where V_{res} and V_{ini} are the residual and impact velocities as given by the simulations, respectively. The ballistic limit V_{50}, the exponent n and the constant A were parameters obtained by least squares fitting.

4. Results and discussion

The following section presents an analysis of the numerical simulations accomplished for the optimisation of the multilayer shield, and summary of numerical results is available in Table 3. Shield configuration, air gap spacing, areal weight, ballistic limit and energy absorbed at the ballistic limit have been included.

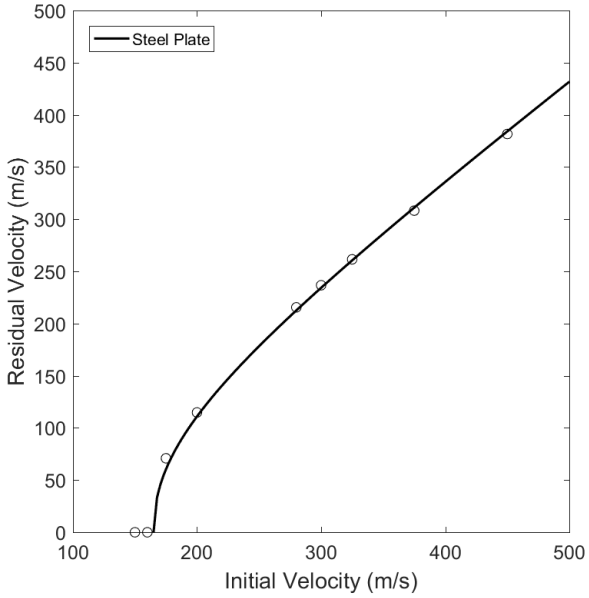

Figure 4: Numerical residual velocity curve of the steel plate with thickness 0.7 mm. The open circles stand for the numerical predictions and the line for eq.9.

4.1. Impact performance of the steel plate

Ballistic response of one single steel plate of 0.7 mm thickness was ascertained by simulation. The results in terms of the residual velocity, V_{res}, as a function of the initial velocity, V_{ini}, are plotted in Fig.4. Ballistic limit was predicted to be 165 m/s, with an energy absorption capacity of 9.6 J for the given projectile. The loss of impact energy was mainly caused by the momentum transfer as a result of the high areal density of the steel plate. Plastic deformation was localised at the impact point and different failure modes were registered for each velocity regime, as previously reported for thin ductile plates stricken by hemispherical projectiles [8]. Low velocity impact resulted in petalling due to the propagation of circumferential cracks preceding the formation of radial cracks, see Fig.5(a). As the impact velocity was further increased, the circumferential cracks produced a clean plug separation from the rest of the plate, see Fig.5(b).

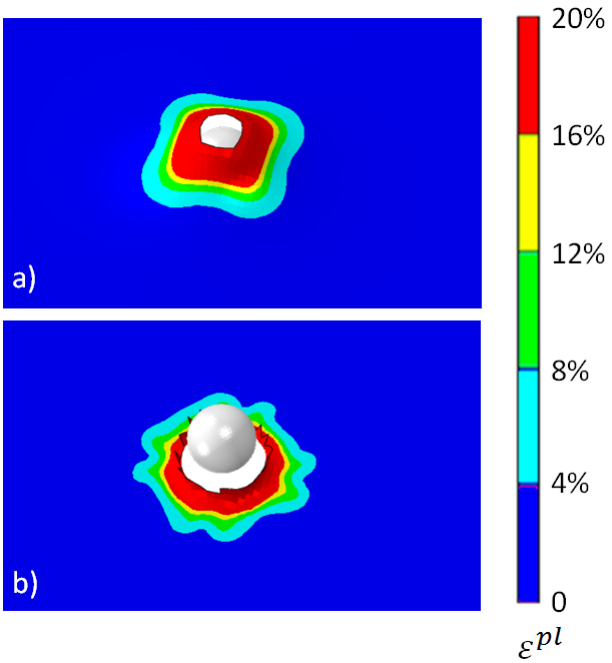

Figure 5: Contour plots of the equivalent plastic strain showing the failure modes of the steel plate for different impact velocity regimes. (a) Petalling failure mode near by the ballistic limit, v_{ini}= 160 m/s at t = 400 μs and (b) shear pluging failure mode for high velocity impact, v_{ini}= 900 m/s at t = 20 μs.

4.2. Impact performance of the nonwoven fabric

The multiscale constitutive model presented above was used to simulate the impact behaviour of the as-received nonwoven fabric at different impact velocities. The results of the simulations, in terms of the residual velocity, V_{res}, as a function of the initial velocity, V_{ini}, are plotted in Fig.6 together with the experimental results presented in [28]. As previously reported [27, 31, 32], the stochastic definition of the fibre pull-out strength promoted a numerical scattering of the predicted residual velocities. The constitutive model was able to capture accurately the ballistic limit of the nonwoven shield and the dominant deformation and failure micromechanisms, however, the numerical simulations tended to underestimate the residual velocity of the projectile above the ballistic limit as failure due to thermal softening of the Dyneema fibres was not included in the model formulation. Maximum energy absorption capacity was characterised as 37.9 J for the given projectile corresponding to a ballistic limit of 328 m/s. Although the nonwoven possessed a higher ballistic limit than

their counterpart steel plate, it presented a relatively low energy absorption capacity above the ballistic limit, characteristic of dry fabrics [9].

The multiscale model replicated the deformation and failure micromechanisms, predicting accurately the wave propagation phenomena during the impact. The model was able to compute the mechanical response of the fabric from the discrete response of the fibres contained in the fibre network, providing detailed evolution of straightening, realignment and sliding for each set of fibre orientations [31]. Energy was dissipated by the tensile deformation of the fabric around the impact point in an elliptical region whose boundaries were controlled by the wave propagation with different velocities along TD and MD, see Fig.7(c). Higher strains appeared at the stiffest direction of the material, as previously reported experimentally during impact on anisotropic plates [39]. The transverse wave was also properly captured, showing the large deformability and low bending stiffness of the material, see Fig.7(a) and (b). The ratio of the major to the minor axis of the cross-section in the simulation was 1.6, close to the experimental value of 2 previously reported [28]. Final penetration of the fabric around the ballistic limit occurred by fibre disentanglement from the fabric network around the impact point, see Fig.8. This failure mechanism, although affected a low fraction of fibres, was able to absorb a significant amount of energy due to the high length of the fibres (50 to 60 mm long).

4.2.1. Influence of the spacing between layers

A detailed study has been carried out to understand the influence of the spacing between layers in the energy absorption capacity of the multilayer nonwoven shield. Numerical models composed by two nonwoven plies positioned at distances ranging from 0.1 to 50 mm every 2 mm were implemented. Predicted residual velocities *vs* spacing between layers for an initial impact velocity of 450 m/s is depicted in Fig.9. Different residual velocities were predicted depending on the interaction between layers. Increasing the spacing between layers, from 0.1 up to 10 mm progressively increased the energy absorption capacity of the target, maintained up to 30 mm spacing. Scatter in energy absorption within this range can be explained considering the variability of the predicted residual velocities observed in

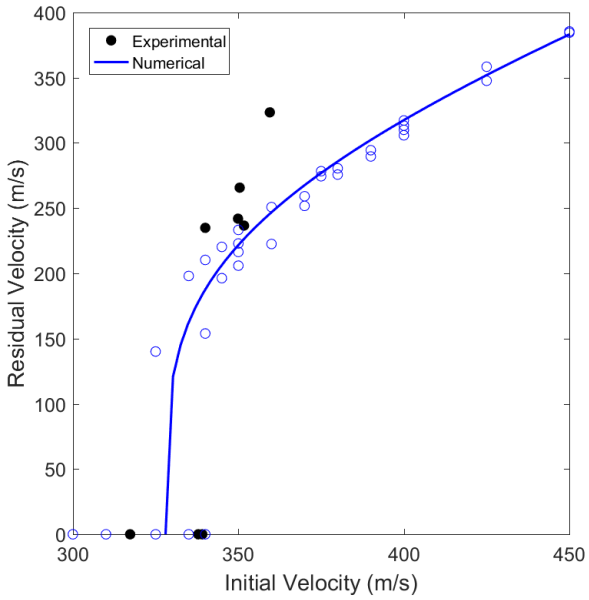

Figure 6: Experimental and numerical residual velocity curves of the nonwoven fabric. The solid circles stand for experimental results, the open circles for the numerical predictions and the line for eq.(9).

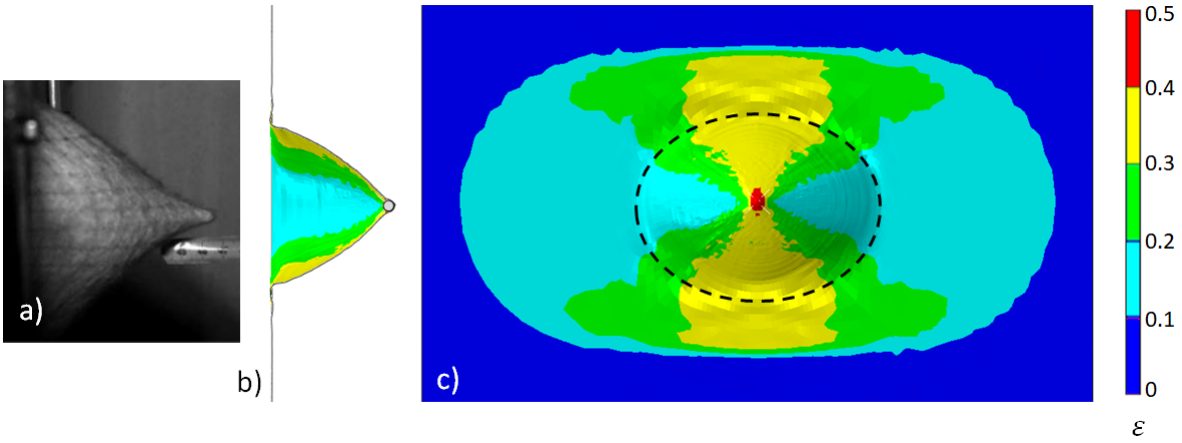

Figure 7: Global deformation of a 350 x 350 mm^2 nonwoven target impacted by a small steel sphere of 5.5 mm diameter. Comparison between (a) experimental deflection and numerical (b) transverse and (c) longitudinal strain waves for the nonwoven fabric impacted at 300 m/s at t = 500 μs, below the ballistic limit. Contour plot of the maximum principal logarithmic strain. The broken line in the figure stand for the boundary of the transverse wave front.

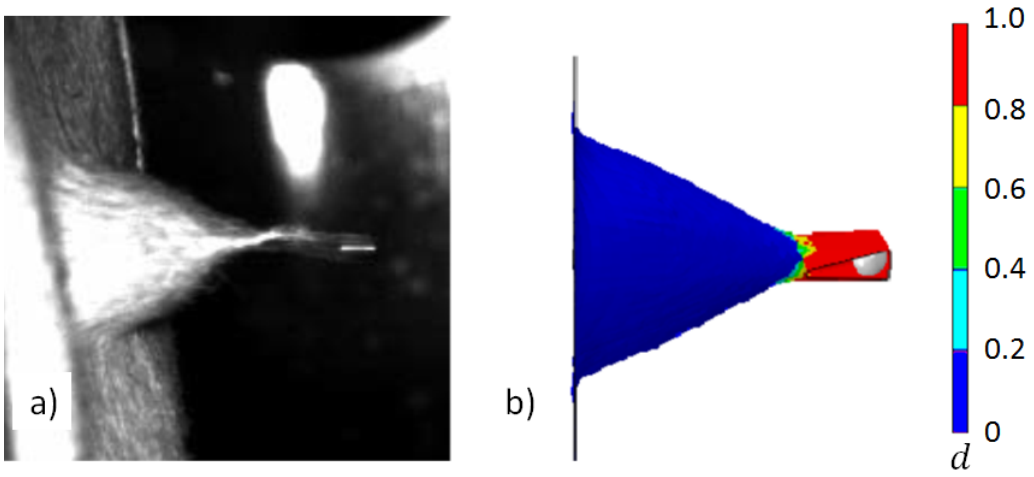

Figure 8: Lateral view of the nonwoven fabric during the impact at 360 m/s at 175 μs above the ballistic limit, leading to the penetration of the fabric, (a) experimental photograph and (b) contour plot of the damage variable. The zones in red in the contour plots are representative of a fully disentangled fabric. [31].

previous publications due to the stochastic implementation of the fibre pull-out strength [31]. Further increment of the gap between layers resulted in a progressive loss of the energy absorption capacity up to 40 mm, where the residual velocity remained constant and independent of this particular design parameter as the physical interaction between plies was prevented. Ballistic curves for 0.1, 10 and 50 mm distance configurations are compared in Fig.10, showing similar trends for residual velocities ranging from 400 to 550 m/s. The response of a single layer has been included as reference. The ballistic limit increased when increasing the areal weight of the shield, however, the maximum ballistic limit was found for the configuration with 10 mm gap, which also presented superior energy absorption capacity for higher impact velocities. Intermediate energy dissipation was found for 0.1 mm spacing, meanwhile, the lower performance appeared for the 50 mm configuration.

Ballistic behaviours were classified in three different categories, depending on the interaction between layers during impact. Ballistic response of the no clearance target (0.1 mm gap) initially behaved as a single layer shield with double density, see Fig.11(a). The interaction between layers became significant once fibre pull-out developed. At this point, higher stresses appeared on the unconstrained rear layer, which failed prematurely due to

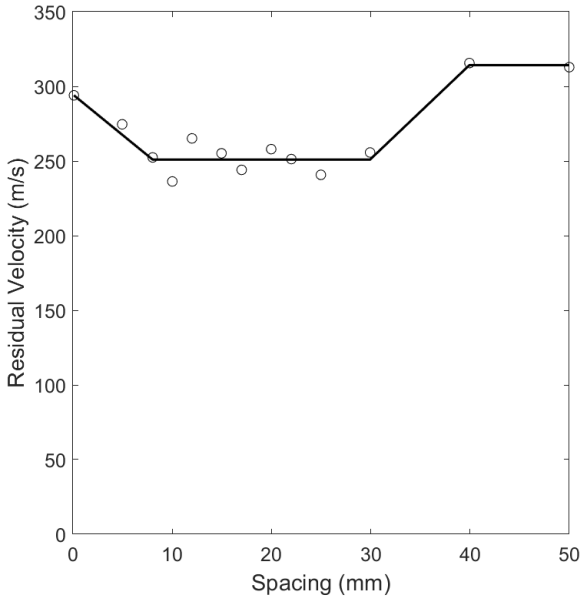

Figure 9: Residual velocity of the projectile *vs* spacing between layers for shields composed by 2 nonwoven layers impacted at 450 m/s. The circles stand for the numerical predictions and the line for the trend curve.

fibre disentanglement, see Fig.11(b). This produced a confinement of the fibres of the front layer, increasing the fibre alignment and energy absorption capacity until final failure of the shield, see Fig.11(c). Similar behaviour in hybrid shields was reported in [32]. As the spacing between layers is progressively increased, a substantial change in the main failure mechanism was observed. For intermediate distances (e. g. 10 mm spacing) in a first stage of the impact, contact of the projectile with the front layer happened, and deformation progressed as observed for the single layer case. As the deflection increased, both layers came in contact and structurally worked together to arrest the projectile, see Fig.11(d). Further deformation initiated the fibre pull-out of the first impacted layer, however, the rear nonwoven, undamaged, contributed to delay the penetration of the first ply, increasing the energy absorbed. After penetration of the front layer, fibre pull-out was induced on the rear layer, see Fig.11(e). Finally the model predicted a total fibre disentanglement, see Fig.11(f). This synergistic contribution was observed up to 30 mm spacing between layers. For configurations with larger gaps, the layer interaction decreased, and beyond 40 mm, the

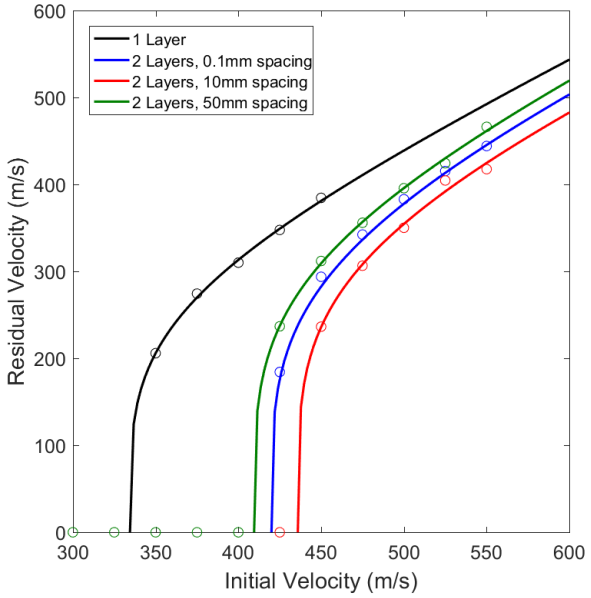

Figure 10: Residual velocity curves for 2 layers nonwoven shields with spacing 0.1, 10 and 50 mm and comparison with the single layer nonwoven. The circles stand for the numerical predictions and the lines for eq.(9).

failure of the layers happened individually, as the front layer failed before contacting the rear one, see Fig.11(h). Therefore, the second layer did not contribute to delay the failure of the first layer and led to a lower impact performance.

The numerical simulations also provided quantitative measurements of the energy absorbed by each layer, justifying the differences in ballistic performance. Fig.12 shows the percentages of strain and kinetic energies transferred to the front and rear layers of the shield during an impact of initial velocity 450 m/s for 0.1, 10 and 50 mm spacing. Evolution of the kinetic energy of the projectile is also depicted for comparison purposes, see Fig.12(e). Frictional dissipation was determined as a 3% of the initial kinetic energy and has not been included in the graphs for the sake of clarity. Artificial energies due to hourglass and element distortion control were maintained below 10% of the total energy of the system. Deformation and failure mechanisms can be analysed through these graphs. On the initial stage of the impact, strain and kinetic energies were homogeneously transmitted to the layers as a result

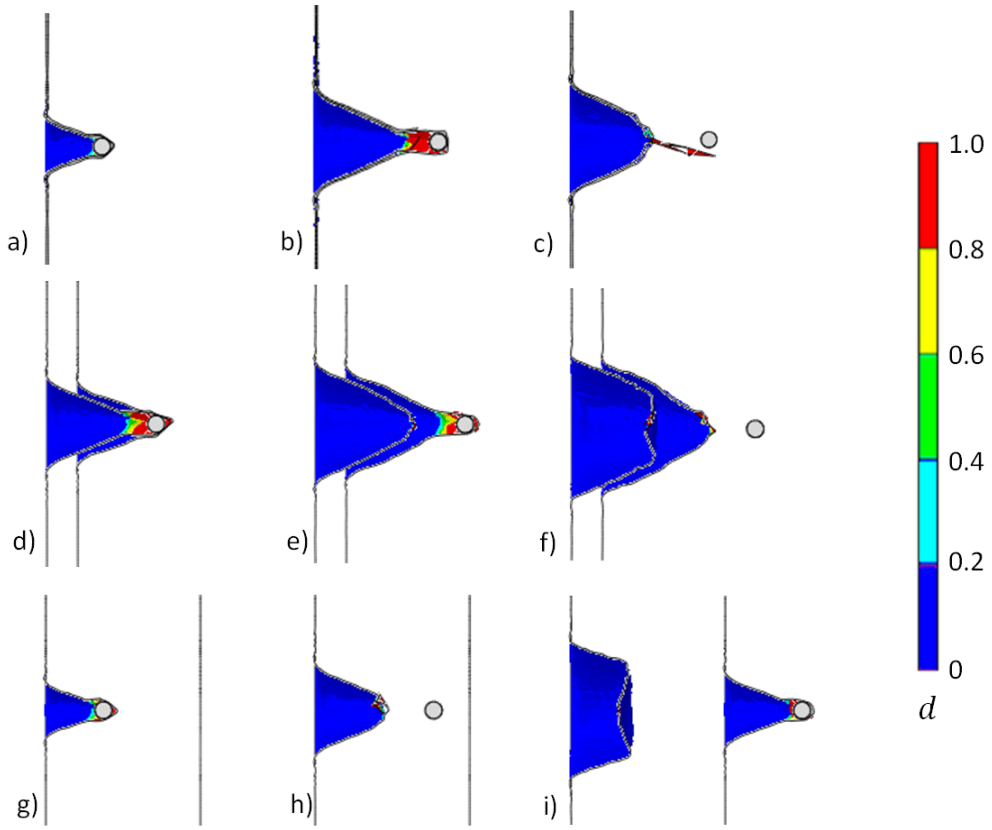

Figure 11: Failure sequence and contour plot of the damage variable for the two-layer shields impacted at 450 m/s. (a), (b) and (c), 0.1 mm spacing at t=50 μs, t=120 μs and t=150 μs, respectively. (d), (e) and (f), 10 mm spacing at t=100 μs, t=150 μs and t=200 μs, respectively. (g), (h) and (i), 50 mm spacing at t=50 μs, t=100 μs and t=200 μs, respectively. The zones in red in the contour plots are representative of a fully disentangled fabric.

of the progressive fibre straightening and alignment produced by the longitudinal and transverse waves. At a certain point of the simulation, pull-out stress threshold of the fibres was overtaken and the projectile produced significant fibre disentanglement. Penetration was virtually represented by element deletion, which generated a release elastic wave, decreasing the stored strain energy, see Figs.12(a) and (b), which was suddenly transformed into an excess of kinetic energy dissipated by viscous damping to avoid numerical instabilities, see Figs.12(c) and (d).

The configuration with 10 mm gap presented higher energy absorption capacity in terms of both strain and kinetic energies, as a result of the beneficial interaction between layers.

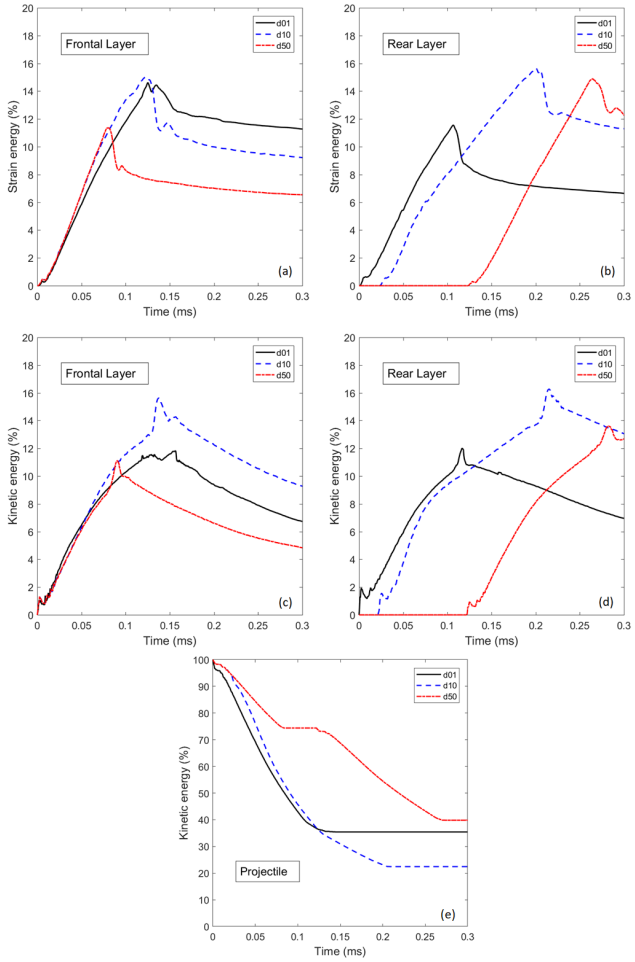

Figure 12: Numerical predictions of the evolution of the energy absorption of the two-layer shields during an impact at 450 m/s with spacing 0.1, 10 and 50 mm. (a), (b) strain energy and (c) and (d) kinetic energy of the front and rear layers, respectively. (e) Evolution of the kinetic energy of the projectile.

Initially the energy absorption rate was similar for all layers in all configurations, as shown by the slopes of the energy evolution curves. As a result of this, the longer the contact time between projectile and shield, the higher the energy absorbed. This fact explains why delaying the final failure of a layer becomes so critical to improve the ballistic performance of the shield. The zero-clearance configuration, 0.1 mm gap, tended to decrease the rate of energy absorption and the momentum transferred as the motion of layers was constrained. At the opposite end, the configuration with the largest gap, 50 mm, worked as two individual systems and presented a premature penetration. Finally, the configuration based on a 10 mm

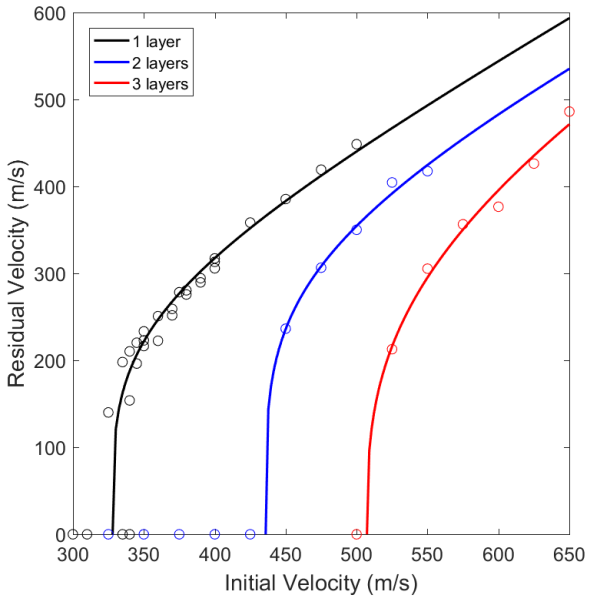

Figure 13: Residual velocity curves for nonwoven targets with 10 mm spacing between layers composed by 1, 2 and 3 layers. The circles stand for the numerical predictions and the lines for eq.(9).

gap distance presented the optimal results due to the synergistic interaction of the layers. Clearly, the rear layer contributed to delay the penetration of the front layer, increasing both, strain and kinetic energies transferred to the target during the impact. Overall, for the given impact energy, this configuration absorbed an additional 12% of energy compared to their counterparts.

Considering the space constraint given by the width of the vehicle door, 10 mm air gap was selected to analyse the response of the three-layer nonwoven shield configuration for future implementation in the automotive component. This distance offered the higher energy absorption capacity (characterised in the region 10 to 30 mm) with the minimum spacing. Fig.13 shows the residual velocity curve together with the single- and two-layered target. Increasing the areal weight of the protection increased the ballistic limit and energy absorption capacity of the shield, up to a maximum of 94.5 J. Failure sequence is reported in Fig.14. The same failure mechanisms as in the previous two-layered configuration were found. Large fibre pull-out was observed, with all layers contributing to delay the final dis-

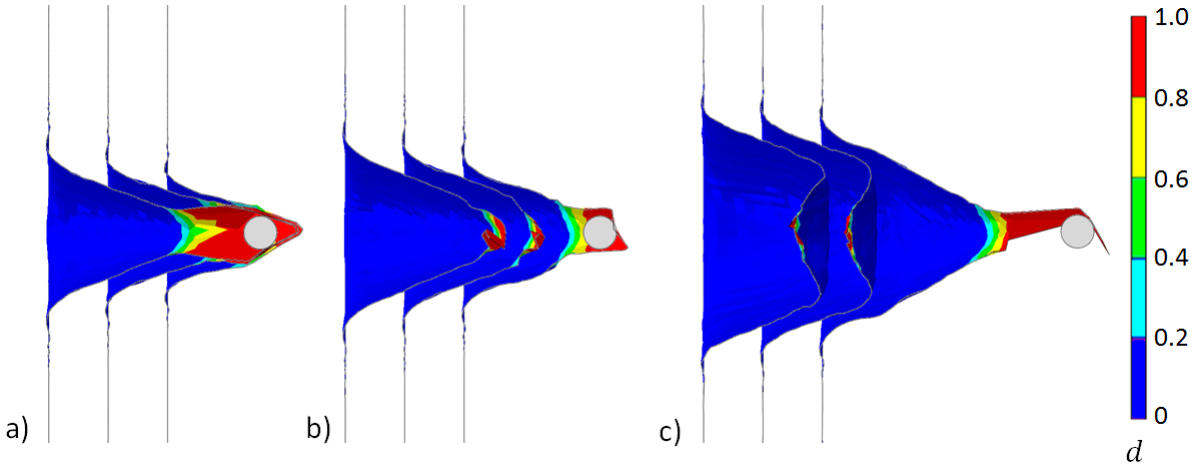

Figure 14: Failure sequence and contour plot of the damage variable for the three-layer shields with 10 mm spacing impacted at 550 m/s. (a) t=80 μs, (b) t=100 μs and (c) t=160 μs. The zones in red in the contour plots are representative of a fully disentangled fabric.

entanglement, see Fig.14(a). As deformation progressed, the frontal and intermediate layers failed simultaneously, see Fig.14(b), with final disentanglement of the rear layer afterwards, as depicted in Fig.14(c).

4.3. Impact performance of multi-layered shields

Finally, the steel plates and nonwoven fabrics were combined in a multi-layered protective shield for automotive applications, and the ballistic performance of the system was evaluated by means of numerical simulations. The shield was composed by two external steel plates and 3 internal nonwovens with a total thickness of 80 mm as specified in Section 3.3. Fig.15 compares the residual velocity curves of the multi-layered target with the performance of its individual components; the steel plates and the nonwoven layers. Although the areal weight of the three nonwovens (600 g/m^2) was about 20 times smaller than the one of the 2 steel plates (11000 g/m^2), a remarkable increment of the ballistic limit of 250 m/s approximately was obtained. Furthermore, the multi-layered system outperformed the previous configurations in terms of ballistic limit and of the energy dissipated, which almost doubled the sum of the energies dissipated individually by the steel plates (19.5 J) and nonwoven fabrics (94.5 J), resulting in an outstanding 195.9J of energy absorption capacity for the given projectile.

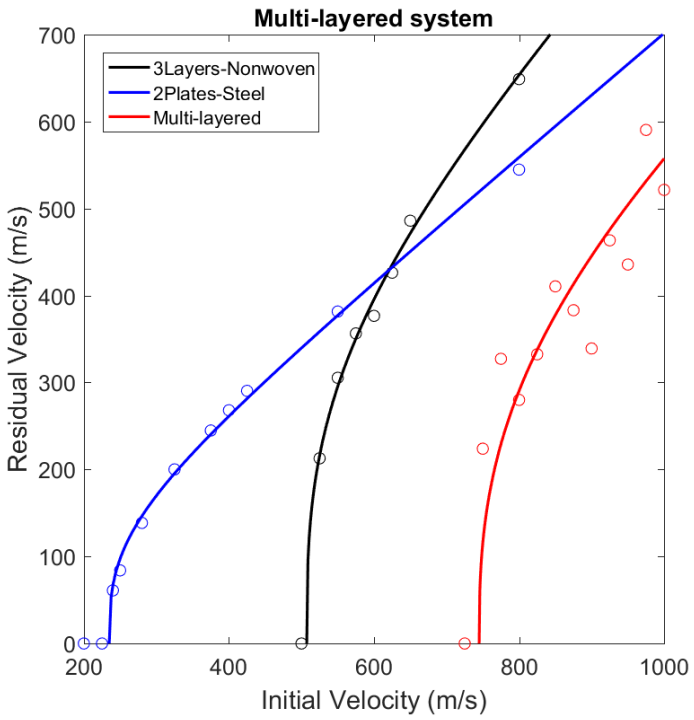

Figure 15: Residual velocity curves for 2 plates of steel (11000 g/m^2 areal weight), 3 layers of nonwoven at 10 mm spacing (600 g/m^2 areal weight) and the combined multi-layered shield composed by the 2 plates plus the 3 intermediate nonwoven layers (11600 g/m^2 areal weight). The circles stand for the numerical predictions and the lines for eq.(9).

It is also worth mentioning that the multi-layered shield increased the energy absorption by a factor over 8 with respect to the steel configuration with a negligible increment of weight of 5.5%.

The large deformation of the nonwoven layers and their synergistic interaction between nonwoven fabrics and metal plates led to this outstanding increment of energy absorption. During the first stage of the impact, the projectile pierced the front steel plate and impacted the nonwoven layers, which deflected together dissipating a significant fraction of the projectile's energy. As it was observed previously for the three- layered shields, the rear nonwoven layers contributed to delay the fibre disentanglement of the front ones, increasing the energy absorbed by all the plies. Further deflection of the layers resulted in the contact of the projectile with the rear steel plate, which not only delayed the failure of the internal

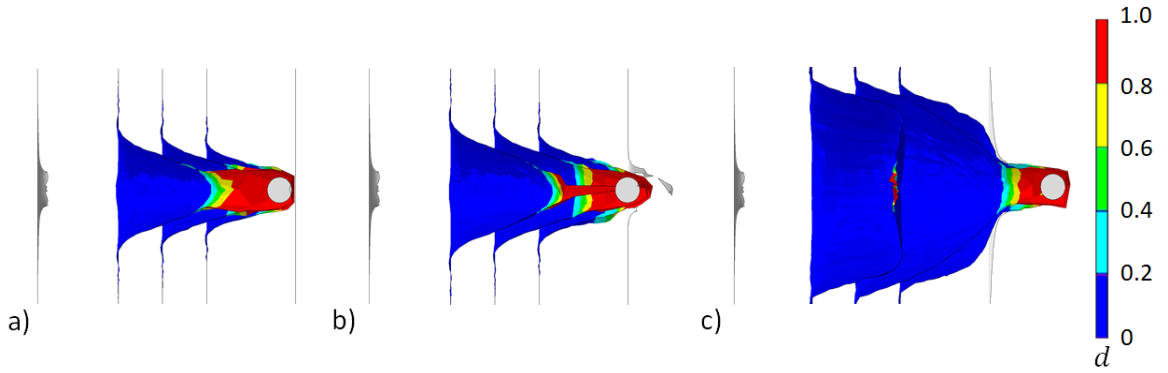

Figure 16: Failure sequence and contour plot of the damage of the multi-layered shield based on two external steel plates and three internal nonwoven layers impacted at 725 m/s. (a) t=90 μs (b) t=135 μs and (c) t=225 μs. The zones in red in the contour plots are representative of a fully disentangled fabric. In this simulation, the projectile was fully arrested after $\approx$ 300 μs.

nonwovens, see Fig.16(a), but also transferred momentum and energy to the plate. The interaction between these nonwovens and the rear plate induced higher plastic deformation on the steel when compared to the front plate. For impact velocities just below the ballistic limit, penetration of the steel plate occurred and the projectile pulled the nonwoven through the generated breach, resulting in a confinement of the material and a massive fibre alignment and rotation towards the loading direction localised at the impact point, see Fig.16(b). This confinement of the nonwoven fabric led to an extra absorption of energy and a progressive decrement of the projectile velocity, which finally got arrested by the ballistic protection, see Fig.16(c).

Although nonwovens absorbed energy by both material deformation and momentum transfer, the metal plates mainly reduced the kinetic energy of the projectile due to the latter mechanism. Fig.17 shows the comparison of the evolution of kinetic energy of the projectile when impacting the baseline metal plates and the hybrid configurations with an impact velocity of 725 m/s. Contact between projectile and layers has been identified by dashed lines. Impact with the steel plates alone produced a sudden drop of the energy of the projectile. Despite this mechanism absorbed a significant amount of energy, it was definitely insufficient to arrest the projectile. On the other hand, the hybrid shield presented a complex

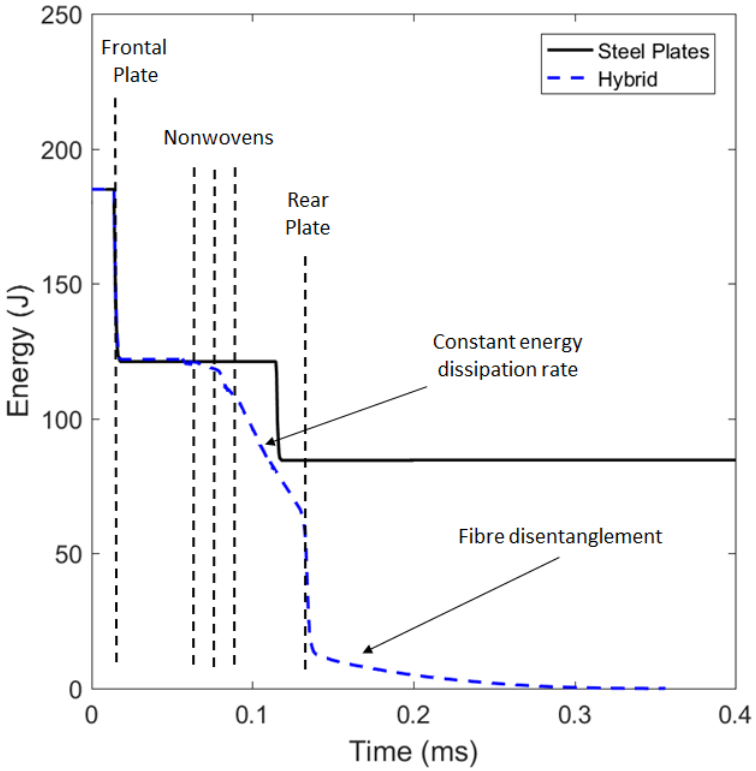

Figure 17: Evolution of the kinetic energy of the projectile when impacting the baseline metal configuration and the hybrid shield with an impact velocity of 725 m/s. The dashed lines indicate the contact points between projectile and layers for the hybrid configuration.

response, that can be divided in four different stages. Initially, the projectile struck the metal plate as in the previous configuration. Afterwards, progressive energy dissipation was controlled by the nonwovens. Energy absorption increased as nonwovens engaged during the impact, resulting in a constant energy dissipation rate over an extended period of time. Further deformation produced the contact with the rear steel plate, inducing a sudden drop of kinetic energy during penetration. The final energy absorption mechanism was fibre disentanglement of the confined material inside the metal plate perforation. Although the fraction of fibres involved in this mechanism was relatively small, the extra time needed for the fibre extraction resulted in a significant energy dissipation, that finally arrested the projectile.

5. Conclusions

The impact response of a hybrid shield composed by external metal plates and internal nonwoven fabrics has been numerically studied. Ballistic performance in terms of residual velocity curves was analysed for impacts with steel spheres of 5.5 mm in diameter for a wide range of initial velocities. Steel plates were modelled by a standard elastic-plastic constitutive law at an homogenised macroscopic level, while the response of the nonwoven fabric was defined by a multiscale constitutive model, able to take into account the complex deformation and fracture mechanisms during impact. Ballistic response of each material was analysed individually. The thin steel plates presented a limited energy absorption capacity due to their low thickness. The main energy absorption mechanism was momentum transfer and plastic deformation, localised at the impact point. The nonwoven fabric presented a higher ballistic limit than the metal plate, although energy absorption capacity was rapidly reduced beyond that point. The identified absorption mechanisms were the momentum transferred to the fabric, fibre realignment and straightening due to the longitudinal wave propagation and fibre pull-out. These findings were in agreement with experimental data previously reported in the literature for both, thin ductile metal plates and nonwovens [8, 31].

Special attention was paid to the interaction between layers for different air gaps in the final energy absorption capacity of the shield. The influence of spacing was analysed for two and three nonwoven layered targets. Intermediate gap distances, between 10 and 30 mm, were beneficial in terms of ballistic limit and final energy absorption. This gap induced a synergistic interaction between layers where the rear ply contributed to delay the final disentanglement of the front layers and therefore produced an increment of the energy transferred to the shield. Quantitatively, the 10 mm gap separation offered an additional 12% of energy dissipation when compared to large gap (50 mm) or no clearance (0.1 mm) configurations. Analysis of the energy absorbed by each layer showed how critical the contact time between projectile and target was to improve the ballistic performance of the shield. Similar failure sequences were observed for the hybrid shield composed by external steel plates and internal nonwoven fabrics. The hybrid system outperformed the previous configurations, resulting in

an outstanding energy absorption capacity, about twice the sum of the energies dissipated by the steel plates and the nonwovens individually. Furthermore, the hybrid shield increased the energy absorption capacity of the baseline steel plates by a factor over 8, with a negligible increment of areal weight of a 5.5%. Thus, this kind of hybrid shields are an efficient lightweight solution to arrest small fragments in the automotive sector. Once again, all the layers of the system contributed to delay the catastrophic failure of the shield increasing the energy absorbed. For velocities close to the ballistic limit, the projectile was able to penetrate the rear steel plate, however, the large deformability of the nonwoven and the extra energy dissipation induced due to the material confinement finally arrested the projectile.

6. Acknowledgement

This investigation was supported by the Universidad Politécnica de Madrid through "Programa Propio 2018" [grant number VJIDOCUPM18ARR]. In addition, FMH acknowledges the support of the University of Edinburgh through the start-up funding for recently appointed Lecturers.

[1] Abtew, M. A., Boussu, F., Bruniaux, P., Loghin, C., Cristian, I., 2019. Ballistic impact mechanisms-a review on textiles and fibre-reinforced composites impact responses. Composite Structures, 110966.

[2] Alderliesten, R., 2015. Designing for damage tolerance in aerospace: A hybrid material technology. Materials & Design 66, 421–428.

[3] ArcelorMittal, 2018. Bake hardening steels.
URL http://corporate.arcelormittal.com/

[4] B. A. Cheeseman, T. A. B., 2003. Ballistic impact into fabric and compliant composite laminates. Composite Structures 61 (1-2), 161–173.

[5] Bansal, S., Mobasher, B., Rajan, S. D., Vintilescu, I., 2009. Development of Fabric Constitutive Behavior for Use in Modeling Engine Fan Blade-Out Events. Journal of Aerospace Engineering 22 (3), 249–259.

[6] Chen, N., Silberstein, M. N., 2019. A micromechanics-based damage model for non-woven fiber networks. International Journal of Solids and Structures 160, 18–31.

[7] Chocron, S., Pintor, A., Cendón, D., Gálvez, F., Sánchez-Gálvez, V., 2002. Simulation of ballistic impact in a polyethylene non-woven felt. In: 20Th Internationa Symposium on Ballistics. Orlando, pp. 23–27.

[8] Corbett, G. G., Reid, I. S. R., Johnson, W., 1996. Impact Loading of Plates and Shells by Free-flying Projectiles: A Review. International Journal of Impact Engineering 18 (2), 141–230.

[9] Cunniff, P. M., 1992. An analysis of the system effects in woven fabrics under ballistic impact. Textile Research Journal 62 (9), 495–509.

[10] Das, A., Tarafder, S., Sivaprasad, S., Chakrabarti, D., 01 2015. Effect of strain rate on bake hardening response of BH220 steel. EPJ Web of Conferences 94, 01037.

[11] Dassault Systemes. Abaqus 6.10 User's Manual, 2010.

[12] Deng, Y., Zhang, W., Cao, Z., 2012. Experimental investigation on the ballistic resistance of monolithic and multi-layered plates against hemispherical-nosed projectiles impact. Materials & Design 41, 266–281.

[13] Destefanis, R., Schäfer, F., Lambert, M., Faraud, M., 2006. Selecting enhanced space debris shields for manned spacecraft. International Journal of Impact Engineering 33 (1-12), 219–230.

[14] Garijo, D., Martínez-Hergueta, F., Lopes, C. S., Llorca, J., González, C., Puente, J. L., Loya, J. A., Toral-Vázquez, J., Votsios, V., Martino, E., 2018. Multiscale FE Modelling and Design of Composite Laminates Under Impact. In: Comprehensive Composite Materials II. Vol. 8. pp. 219–238.

[15] Guo, Y. B., Chiang, H. J., Deng, J. J., Shim, V. P., 2019. Projectile impact on fabric-metal assemblies Influence of fabric-metal sequence. International Journal of Impact Engineering 127 (December 2018), 1–16.

[16] He, Z., Xuan, H., Bai, C., Hu, Y., Cong, P., Bai, H., 2017. Containment tests and analysis of soft wall casing fabricated by wrapping Kevlar fabric around thin metal ring. Aerospace Science and Technology 61, 35–44.

[17] Hooputra, H., Gese, H., Dell, H., Werner, H., 2004. A comprehensive failure model for crashworthiness simulation of aluminium extrusions. International Journal of Crashworthiness 9 (5), 449–464.

[18] Ipson, T. W., Wittrock, E. P., 1966. Response of non-woven synthetic fiber textiles to ballistic impact. Tech. rep., No. TR-67-8-CM. Denver Research Institute.

[19] Kiliç, N., Ekici, B., 2013. Ballistic resistance of high hardness armor steels against 7 . 62 mm armor piercing ammunition. Materials and Design 44, 35–48.

[20] Kiran, R., Khandelwal, K., 2014. A triaxiality and lode parameter dependent ductile fracture criterion. Engineering Fracture Mechanics 128, 121–138.

[21] Krishnan, K., Sockalingam, S., Bansal, S., Rajan, S. D., 2010. Numerical simulation of ceramic composite armor subjected to ballistic impact. Composites Part B: Engineering 41 (8), 583–593.

[22] Lambert, J., Jonas, G., 1976. Towards standardization in terminal ballistics testing: velocity representation. Tech. rep., Army Ballistic Research Lab. Aberdeen.

[23] Lim, C., Shim, V., Ng, Y., 2003. Finite-element modeling of the ballistic impact of fabric armor.

International Journal of Impact Engineering 28 (1), 13–31.

[24] Liu, J., Long, Y., Ji, C., Liu, Q., Zhong, M., Zhou, Y., 2018. Influence of layer number and air gap on the ballistic performance of multi-layered targets subjected to high velocity impact by copper EFP. International Journal of Impact Engineering 112, 52–65.

[25] Liu, P., Zhu, D., Yao, Y., Wang, J., Bui, T. Q., 2016. Numerical simulation of ballistic impact behavior of bio-inspired scale-like protection system. Materials & Design 99, 201–210.

[26] Marino, M., Wriggers, P., 2019. Micro–macro constitutive modeling and finite element analytical-based formulations for fibrous materials: A multiscale structural approach for crimped fibers. Computer Methods in Applied Mechanics and Engineering 344, 938–969.

[27] Martínez-Hergueta, F., 2016. Multiscale analysis of the mechanical behavior of needle-punched nonwoven fabrics. Ph.D. thesis, Polytechnic University of Madrid.

[28] Martínez-Hergueta, F., Ridruejo, A., Gálvez, F., González, C., LLorca, J., 2016. Influence of fiber orientation on the ballistic performance of needlepunched nonwoven fabrics. Mechanics of Materials 94, 106–116.

[29] Martínez-Hergueta, F., Ridruejo, A., González, C., LLorca, J., 2015. Deformation and energy dissipation mechanisms of needle-punched nonwoven fabrics: A multiscale experimental analysis. International Journal of Solids and Structures 65, 120–131.

[30] Martínez-Hergueta, F., Ridruejo, A., González, C., LLorca, J., 2016. Multiscale micromechanical model for needlepunched nonwoven fabrics. International Journal of Solids and Structures 96, 81–91.

[31] Martínez-Hergueta, F., Ridruejo, A., González, C., Llorca, J., 2017. Numerical simulation of the ballistic response of needle-punched nonwoven fabrics. International Journal of Solids and Structures 106-107, 56–67.

[32] Martínez-Hergueta, F., Ridruejo, A., González, C., LLorca, J., 2018. Ballistic performance of hybrid nonwoven/woven polyethylene fabric shields. International Journal of Impact Engineering 111, 55–65.

[33] Naik, D., Sankaran, S., Mobasher, B., Rajan, S., Pereira, J., 2009. Development of reliable modeling methodologies for fan blade out containment analysis Part I: Experimental studies. International Journal of Impact Engineering 36 (1), 1–11.

[34] Pandya, K. S., Pothnis, J. R., Ravikumar, G., Naik, N., 2013. Ballistic impact behavior of hybrid composites. Materials & Design 44, 128–135.

[35] Qiao, P., Yang, M., Bobaru, F., 2008. Impact Mechanics and High-Energy Absorbing Materials :Review. Journal of Aerospace Engineering 21 (October), 235–248.

[36] Ridruejo, A., González, C., LLorca, J., 2012. A constitutive model for the in-plane mechanical behavior of nonwoven fabrics. International Journal of Solids and Structures 49 (17), 2215–2229.

[37] Russell, S. J., 2007. Handbook of nonwovens. The Textile Institute. Woodhead Publishing.

[38] Sadighi, M., Alderliesten, R. C., Benedictus, R., 2012. Impact resistance of fiber-metal laminates: A review. International Journal of Impact Engineering 49, 77–90.

[39] Seidt, J. D., Pereira, J. M., Gilat, A., Revilock, D. M., Nandwana, K., 2013. Ballistic impact of anisotropic 2024 aluminum sheet and plate. International Journal of Impact Engineering 62, 27–34.

[40] Shen, C., Dumbleton, J., 1974. The friction and wear behavior of irradiated very high molecular weight polyethylene. Wear 30 (3), 349–364.

[41] Shim, V., Tan, V., Tay, T., 1995. Modelling deformation and damage characteristics of woven fabric under small projectile impact. International Journal of Impact Engineering 16 (4), 585–605.

[42] Shockey, D. A., Erlich, D. C., Simons, J. W., 1999. Lightweight Fragment Barriers for Commercial Aircraft. 18Th International Symposium on Ballistics, 15–19.

[43] Sinmazçelik, T., Avcu, E., Özgür, M., Çoban, O., 2011. A review: Fibre metal laminates, background, bonding types and applied test methods. Materials and Design 32, 3671–3685.

[44] Stahlecker, Z., Mobasher, B., Rajan, S., Pereira, J., 2009. Development of reliable modeling methodologies for engine fan blade out containment analysis. Part II: Finite element analysis. International Journal of Impact Engineering 36 (3), 447–459.

[45] Tabiei, A., Nilakantan, G., 2008. Ballistic impact of dry woven fabric composites: A review. Applied Mechanics Reviews 61 (1), 010801.

[46] Thoma, K., Schäfer, F., Hiermaier, S., Schneider, E., 2004. An approach to achieve progress in spacecraft shielding. Advances in Space Research 34 (5), 1063–1075.

[47] Thomas, H. L., Bhatnagar, A., Wagner, L. L., 2003. Needle-Punched Non-Woven for High Fragment Protection. In: 14th International Conference of Composite Materials. San Diego, California.

[48] Vila-Ortega, J., 2018. Simulation of the ballistic impact on multilayer polyethylene nonwoven system. Master's thesis, Technical University of Madrid.

[49] Wang, Q., Chen, Z., Chen, Z., 2013. Design and characteristics of hybrid composite armor subjected to projectile impact. Materials & Design 46, 634–639.

[50] Yaghoubi, A. S., Liaw, B., 2012. Thickness influence on ballistic impact behaviors of GLARE 5 fiber-metal laminated beams : Experimental and numerical studies. Composite Structures 94 (8), 2585–2598.